

Cite this: *J. Mater. Chem. C*, 2021,  
9, 3871

# Ion and hole dual-channel transport columnar mesomorphic organic electronic materials with high anisotropic conductivities based on supramolecular discotic ionic liquid crystals†

Jian Chen,<sup>‡a</sup> Yuhao Sun,<sup>‡a</sup> Weiguang Zhao,<sup>a</sup> Jiang Liu,<sup>a</sup> Jianglin Fang,<sup>b</sup> Tianchi Xu<sup>\*a</sup>  
and Dongzhong Chen<sup>ib</sup><sup>\*a</sup>

Thermotropic ionic liquid crystals (ILCs) are a kind of fascinating functional organic material combining the characteristics and advantages of both liquid crystals (LC) and ionic liquids. Here in this work, a series of supramolecular discotic ILCs of C<sub>n</sub>-tri-CTP have been produced through host-guest complexation together with  $\pi$ - $\pi$  stacking and electrostatic interactions between the readily prepared electrically neutral tris(18-crown-6)triphenylene (tri-CTP) and the readily available potassium trialkoxybenzenesulfonates with different length alkyl tails of carbon number  $n = 8, 10, 12, 14, 16$ . The thus obtained ILC complexes show enantiotropic ordered columnar mesophases, such as center-faced rectangular columnar (Col<sub>f</sub>) and oblique columnar (Col<sub>ob</sub>) mesophases with broad LC temperature ranges and excellent thermal stability. It is very interesting and fascinating to find that after a simple alignment, such supramolecular discotic ILC complexes in their ordered columnar structures achieve simultaneously anisotropic ionic conductivities as high as  $1.99 \times 10^{-2} \text{ S cm}^{-1}$  and hole mobility reaching  $4.6 \times 10^{-2} \text{ cm}^2 \text{ V}^{-1} \text{ s}^{-1}$ , thus exhibiting fantastic dual-channel transport properties both for ions and holes, which may develop into a kind of versatile organic electronic material for various promising unique applications.

Received 17th October 2020,  
Accepted 3rd February 2021

DOI: 10.1039/d0tc04931j

rsc.li/materials-c

## Introduction

Thermotropic ionic liquid crystals (ILCs) are fascinating functional organic materials, which integrate the self-assembly characteristics and molecular orientational order of liquid crystals (LCs) with ionic conductivity and other advantages of ionic liquids.<sup>1–8</sup> Various columnar organizations of discotic LC semiconductors endow them with energy/charge transport characteristics along the pseudo one-dimensional (1D) columnar direction, thus bearing broad attractive applications in nanotechnology and organic optoelectronics.<sup>9–15</sup> It showed that realizing efficient transport and high charge carrier mobilities in discotic LC semiconducting materials was not only closely related to the central aromatic core, but also various molecular design or structural

modifications played a pivotal role such as different spacers between the aromatic core and alkyl tails, introducing polar groups, hydrogen bonding and metal coordination,<sup>16–23</sup> which increased the intramolecular and intermolecular order and at the same time reduced the stacking distance. Some discotic ILCs have been reported to be capable of forming characteristic columnar structures and combining the ionic transport and electronic conduction potentials as a kind of fascinating versatile organic semiconductor.<sup>5–8,24–33</sup> The exploration of covalently bonded discotic ILCs has been limited because of their usually complicated synthesis and complex purification procedures for the charged discotic aromatic moieties,<sup>5–8</sup> while noncovalent supramolecular approaches markedly simplify the synthesis procedure, which can also show some particular functions and expanded applications.<sup>34,35</sup> Kato and coworkers demonstrated that noncovalent design exhibited significantly enhanced ionic conductivities in nanosegregated columnar LCs in virtue of the increased mobility of the ionic moieties.<sup>8,36</sup>

Crown ether has been playing a key role in supramolecular assemblies *via* host-guest interactions.<sup>37–39</sup> A range of crown ether modified disc-like derivatives have already been reported, with alkali cations or some onium salts employed for regulating their association behaviors in solution<sup>40–42</sup> or self-organized superstructures in the bulk state.<sup>43–50</sup> However, so far in most

<sup>a</sup> Key Laboratory of High Performance Polymer Materials and Technology of Ministry of Education, Collaborative Innovation Center of Chemistry for Life Sciences, Department of Polymer Science and Engineering, School of Chemistry and Chemical Engineering, Nanjing University, Nanjing 210023, China. E-mail: cdz@nju.edu.cn, xtc@nju.edu.cn

<sup>b</sup> Center for Materials Analysis, Nanjing University, Nanjing 210093, China

† Electronic supplementary information (ESI) available: Synthesis and characterization of building blocks and some supplementary figures and tables. See DOI: 10.1039/d0tc04931j

‡ These authors contributed equally to this work.

of the reported cases the decorated crown ether macrocycles were usually located in the middle part with different number alkoxy substituents covalently linked to the attached aromatic moieties, exhibiting applications such as sensing for various characteristic ions.<sup>40–47</sup> Among these crown ether involved discotic ILCs, triphenylene (TP) is among the most widely adopted discotic cores.<sup>43–46,50</sup> On the other hand, tapered or wedge-shaped benzenesulfonates have been often employed for the construction of ILCs through nanosegregated disc-like stacking.<sup>51–55</sup> Very recently, we reported a rational supramolecular strategy for constructing discotic ILCs *via* crown ether based host–guest complexation from facily synthesized tris(18-crown-6)triphenylene and potassium of mono- or di-alkyl substituted benzenesulfonates.<sup>56</sup> This is the first example from the easily accessible electrically neutral tri-crown-ether triphenylene (tri-CTP) and potassium benzenesulfonates through host–guest interactions to show rich phases of three-dimensional (3D) cubic solid crystals, and 2D columnar and 1D lamellar LC mesophases and predict that the 2D ordered columnar LC mesophases may serve as promising organic electronic materials both for electron and ion transport.<sup>56</sup> However, in spite of their abundant phase behavior characteristics, most of the complexes from tri-CTP and potassium benzenesulfonates with mono- or di-substituted alkyl tails developed only monotropic LC mesophases with narrower temperature ranges.<sup>56</sup> What's more, such complexes from mono- or di-alkyl substituted benzenesulfonates exhibited poor thermal stability with partial decomposition in each thermal cycle thus severely limiting their significance and application possibilities, which implied the direction for our next effort and promoted our further intensified study to boost potential unique organic electronic applications.

In this work, with the readily prepared electrically neutral tri-CTP as the host, a set of supramolecular discotic ILCs have been constructed through host–guest interactions with the facily available potassium trialkoxybenzenesulfonate derivatives of different length alkyl tails. The thus obtained discotic ILCs exhibited enantropic ordered columnar mesophases with significantly broadened LC temperature ranges and excellent thermal stability thanks to the increase in the proportion of nonpolar flexible alkyl moieties and synergistic enhancement through host–guest recognition, electrostatic interactions and  $\pi$ - $\pi$  stacking. Moreover, three crown ether rings surrounding the TP core constituted the ion migration channel and greatly reduced the 1D transport resistance of potassium cations to achieve a quite high ionic conductivity meeting the critical requirement for solid electrolytes in battery applications. Together with the measured rather high hole mobilities, such supramolecular discotic ILCs with dual-channel transport capabilities both for ions and holes are promising to be applied as novel functional organic electronic materials in various fields.

## Results and discussion

### Building supramolecular ILCs from host–guest complexation

As shown in Fig. 1, discotic ILCs from tri-CTP of tris(18-crown-6)triphenylene and potassium benzenesulfonates with mono- or

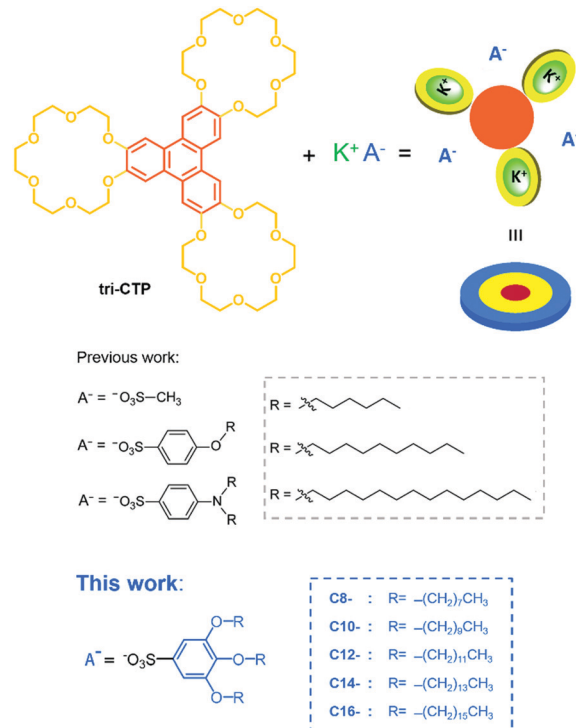


Fig. 1 Schematic illustration and comparison of supramolecular ILCs based on host–guest interactions between tri-CTP and potassium benzenesulfonates with mono- or di-alkyl substituted tails as previously reported by our group and by adopting the facily available potassium trialkoxybenzenesulfonates with different length alkyl tails in this work.

di-alkyl substituted tails were first constructed *via* host–guest interactions as recently reported in our previous work, which exhibited only monotropic LC mesophases, showing obvious thermal instability and greatly limiting their application potential. In this work, based on the easily obtainable and inexpensive potassium trialkoxybenzenesulfonates with different length alkyl tails and the same electrically neutral tri-CTP, well-organized discotic ILCs have been achieved, showing enantropic ordered columnar mesophases with excellent thermal stability.

The host–guest complexes were prepared just by simply solution mixing the host tri-CTP composed of the aromatic TP core with three peripheral crown ether rings and slightly excessive guest compounds of potassium trialkoxybenzenesulfonates with variant length alkyl tails of carbon number  $n = 8, 10, 12, 14, 16$  (denoted as C8, C10, C12, C14 and C16, respectively) in dichloromethane. After evaporation of the solvent at room temperature, the obtained solid mixture was co-dissolved in methanol and precipitated in deionized water; the dissolution/precipitation procedure was repeated three to four times to completely remove the excessive guest molecule. The composition and the stoichiometric ionic LC complexes in a host/guest ratio of 1:3 were confirmed by the characteristic  $^1\text{H}$  NMR spectra, wherein the integral area ratio of the aromatic proton signals resulting from the TP core and from the benzene ring of the associated guest trialkoxybenzenesulfonate was exactly 1:1, denoted as **a** at around 7.83 and **g** at around 7.11, respectively, for the representative complex C12-tri-CTP (Fig. 2a). As compared with that from the neat host component tri-CTP,

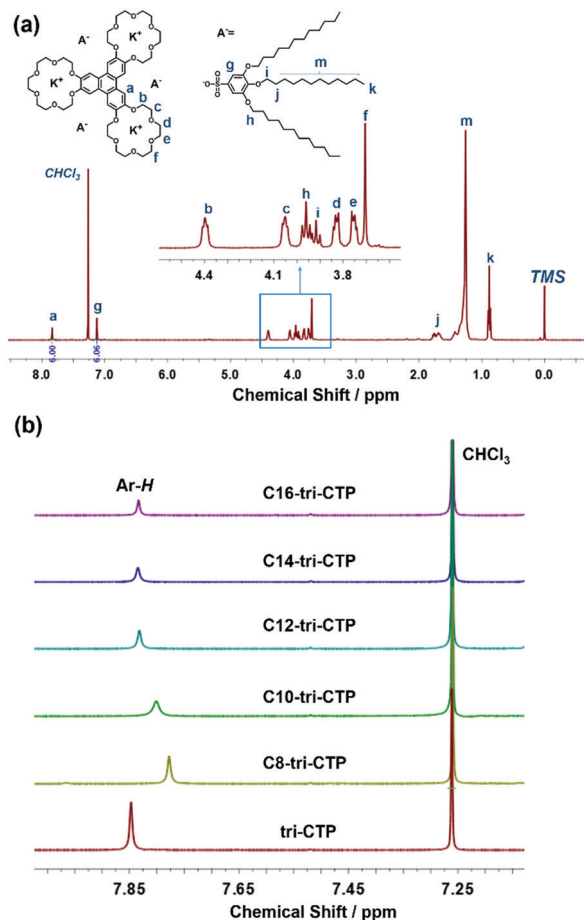


Fig. 2 (a) The typical  $^1\text{H}$  NMR spectrum of the representative complex C12-tri-CTP in  $\text{CDCl}_3$ . (b) Comparison of the TP aromatic proton chemical shifts in the  $^1\text{H}$  NMR spectra of the series of supramolecular LC complexes  $C_n$ -tri-CTP ( $n = 8, 10, 12, 14, 16$ ) and of the neat host molecule tri-CTP.

the peaks of the aromatic TP proton (Ar-H) in the supramolecular LC complexes slightly shifted to a higher field (Fig. 2b), which was attributed to the shielding effect of the ionic pair formed by a sulfonate anion and a potassium cation bounded to the crown ether of tri-CTP.<sup>56</sup> Moreover, a more significant shift was exhibited by complexes C8-tri-CTP and C10-tri-CTP with relatively short alkoxy substituents, which implied the reduced ion pair effect with the lowered proportion of the ionic moieties for those  $C_n$ -tri-CTP ( $n = 12, 14, 16$ ) with extended length alkyl tails and thus increased van der Waals interactions.

## Thermal properties and phase behaviors

The thermal properties and phase behaviors of the prepared ILCs were investigated and comprehensively analyzed by a combination of thermal gravimetric analysis (TGA), differential scanning calorimetry (DSC), polarized optical microscopy (POM) and small/wide angle X-ray scattering (SAXS/WAXS), as summarized in Table 1.

The supramolecular ILC complex series exhibited high thermal stability. The temperatures of 5% weight loss ( $T_{5\%}$ ) both for C8-tri-CTP and C10-tri-CTP were around 210 °C, with the decomposition temperature of about 250 °C. Those with longer alkyl tails of C12-tri-CTP, C14-tri-CTP and C16-tri-CTP showed more enhanced thermal stability, with  $T_{5\%}$  of at least 10 K higher than that of those analogues with shorter tails. Among them, C12-tri-CTP displayed exceptionally high thermal stability with  $T_{5\%}$  reaching 267 °C (Fig. S11, ESI<sup>†</sup>). DSC thermal analyses together with POM observations were employed for the determination of phase transition temperatures. Almost all the series of complex samples exhibited a crystal melting peak at around 30–50 °C in the 2nd heating DSC traces and a corresponding crystallization exothermic transition during the cooling scan with some degree supercooling, and also a weak high-temperature phase transition peak at more than 100 °C with a smaller enthalpy change (Fig. S12, ESI<sup>†</sup>). Except that C8-tri-CTP with the shortest alkyl tails did not show any melting peak during DSC scans, crystallization occurring was confirmed from POM observation, which was conducted at a slower heating/cooling rate. For the high-temperature phase transitions, compared to the other homologues, C12-tri-CTP showed significantly enhanced peaks, which are related to their crystallization dominated specific phase behaviors as discussed next. POM investigations manifested that during gradual cooling from the isotropic state, obvious birefringence with atypical mosaic-like textures were observed for the series of complexes in their LC mesophases (Fig. S13, ESI<sup>†</sup>), except that the C12-tri-CTP complex always showed feathered fan-shaped or focal conical fan-like crystalline textures even persistent to higher temperatures consistent with those from DSC analysis, manifesting the transition between different crystalline forms of C12-tri-CTP with polymorphism until the isotropization into a melting liquid state showing a dark field (Fig. S14, ESI<sup>†</sup>). Upon reaching ambient temperature in the crystalline state, C8-tri-CTP and C10-tri-CTP exhibited needle-like textures, while C14-tri-CTP and C16-tri-CTP exhibited spherulite

Table 1 Thermotropic phase behaviors and associated structures of the series of supramolecular ILCs of  $C_n$ -tri-CTP ( $n = 8, 10, 12, 14, 16$ )

Complex code	Thermal transitions/°C (enthalpy changes/J g <sup>-1</sup> ) <sup>a</sup>		$T_{5\%}/^{\circ}\text{C}^c$
	Second heating <sup>b</sup>	First cooling <sup>b</sup>	
C8-tri-CTP	Cr 52 <sup>d</sup> M <sub>x</sub> 126(35.2) Iso	Iso 115 <sup>d</sup> M <sub>x</sub> 44 <sup>d</sup> Cr	207
C10-tri-CTP	Cr 56(17.4) Col <sub>r</sub> 101(2.6) Iso	Iso 88 <sup>d</sup> Col <sub>r</sub> 48(11.9) Cr	208
C12-tri-CTP	Cr <sub>1</sub> 38(109.8) Cr <sub>2</sub> 149(21.0) Cr <sub>3</sub> 174(98.3) Iso	Iso 143(16.8) Cr <sub>3</sub> 128(71.5) Cr <sub>2</sub> 10(67.8) Cr <sub>1</sub>	267
C14-tri-CTP	Cr 40(250.5) Col <sub>ob</sub> 158(17.7) Iso	Iso 103(39.2) Col <sub>ob</sub> 34(201.2) Cr	225
C16-tri-CTP	Cr 54(543.4) Col <sub>ob</sub> 159(24.6) Iso	Iso 107(32.8) Col <sub>ob</sub> 50(504.4) Cr	218

<sup>a</sup> Cr, crystal phase; M<sub>x</sub>, undefined mesophase; Col<sub>r</sub>, center-faced rectangular columnar LC mesophase; Col<sub>ob</sub>, oblique columnar LC mesophase; Iso, isotropic state. <sup>b</sup> Heating or cooling rate at 10 °C min<sup>-1</sup>. <sup>c</sup> From TGA. <sup>d</sup> Determined from POM observation.

crystalline textures (Fig. S13, ESI†). It is worth noting that unlike the polycrystalline C12-tri-CTP could not be sheared until near the isotropization temperature, all other analogous complexes of  $C_n$ -tri-CTP ( $n = 8, 10, 14, 16$ ) showed fluidity in their LC temperature ranges as demonstrated with quite uniform alignment after shearing at 70 °C, exhibiting distinctly different shear-aligned POM images (Fig. S15, ESI†) in contrast to those before shearing (the left column in Fig. S13, ESI†).

### Self-organized structures

Variable temperature SAXS/WAXS analysis is a powerful tool for investigating and elucidating the organized structures. In general, all the complexes showed typical crystalline diffraction characteristics of multiple sharp peaks at room temperature due to the crystallization of the peripheral alkyl tails or the complex as a whole (Fig. S16, ESI†). As shown in Fig. 3, at higher temperatures, all other complexes exhibited different LC columnar mesophases with a perceptible small peak at around  $q = 14.5 \text{ nm}^{-1}$  presumably ascribed to the partial crystallization of alkyl chains, except that C12-tri-CTP showed the crystalline state of various polycrystalline forms in different temperature ranges with characteristic multiple sharp peaks until above the clearing point (here, the highest melting temperature). Specifically, for C10-tri-CTP at 80 °C in the LC state, all the 2D Miller indices ( $hk$ ) satisfied  $h + k = 2m$  ( $m = 1, 2, 3, \dots$ ), which indicated a center-faced rectangular columnar LC mesophase ( $\text{Col}_r$ ,  $C2mm$ ) with lattice parameters of  $a = 4.70 \text{ nm}$  and  $b = 4.35 \text{ nm}$  (Fig. 3b, and Fig. S17, Table S1, ESI†). The phase behavior of C8-tri-CTP was to some extent similar to that of C10-tri-CTP, while it was much less organized and not sufficient to clearly determine its phase structure due to few scattering peaks and weak signal intensities. For those with

longer alkyl tails of C14-tri-CTP and C16-tri-CTP at 80 °C, both exhibited LC mesophases of an oblique columnar structure ( $P2$ ) with lattice parameters of  $a = 4.03 \text{ nm}$ ,  $b = 3.50 \text{ nm}$ , and  $\theta = 60^\circ$  and  $a = 5.23 \text{ nm}$ ,  $b = 3.62 \text{ nm}$ , and  $\theta = 56.5^\circ$ , respectively (Fig. 3d, e, and Fig. S18, S19, Tables S2 and S3, ESI†). For those complexes showing columnar mesophases, such as C10-tri-CTP, C14-tri-CTP and C16-tri-CTP, the distance between two adjacent tri-CTP cores was determined from SAXS/WAXS analysis to be 0.35 nm (Tables S1–S3, ESI†), comparable to or even closer than the typical  $\pi$ -stacking distance in the TP-based columnar structures,<sup>14,15</sup> indicating that the introduction of guests in the complexes did not significantly perturb the stacking of the aromatic TP cores. Instead, such a kind of supramolecular complexation promoted noticeably the organization and packing of columnar structures as effective as the reported various molecular design or structural modification strategies,<sup>16–23</sup> which constituted the structural basis for their electron/hole transport together with the ionic conductance of the crown/ $\text{K}^+$  channel, contributing to their dual-channel transport properties as discussed next. It is worth mentioning that the calculated density of  $1.36 \text{ g cm}^{-3}$  and  $1.33 \text{ g cm}^{-3}$ , respectively, for the ionic complexes C10-tri-CTP and C14-tri-CTP (Tables S1 and S2, ESI†) seemed to be slightly higher than the common density values for organic solid materials, while the densities of ionic complexes of triphenylene-substituted crown ether complexed with  $\text{K}^+$  were calculated to be higher than  $1.2 \text{ g cm}^{-3}$ .<sup>44</sup> Moreover, in the ionic complexes of semifluorinated tapered monodendrons containing crown ethers reported by Percec and coworkers in various columnar mesophases, the measured densities were even higher than  $1.4 \text{ g cm}^{-3}$ , attributed to ion complexation, fluorine substitution and the ordered regular stacking.<sup>57</sup> The 2D discotic columnar mesophases and packing structures of the series of ionic LC complexes are illustrated in Fig. 4.

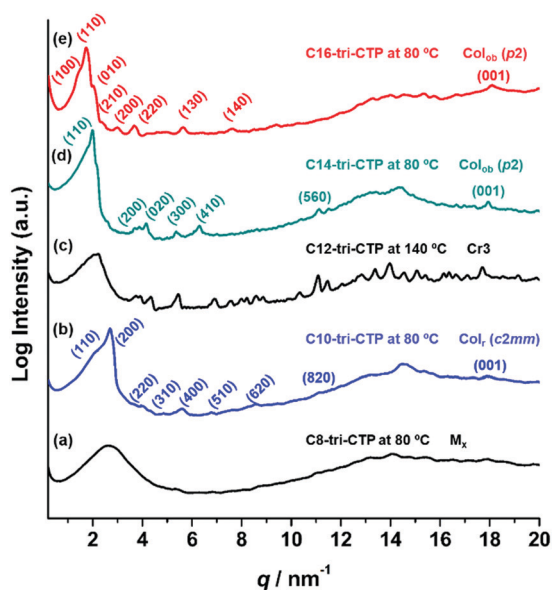


Fig. 3 SAXS/WAXS profiles of the series of complexes at indicated temperatures with assigned phases. (a) C8-tri-CTP assigned as an undefined mesophase ( $M_x$ ) at 80 °C due to limited effective signals, (b) C10-tri-CTP at 80 °C in  $\text{Col}_r$ , (c) C12-tri-CTP in the crystalline state persistent to high temperatures, (d) C14-tri-CTP at 80 °C in  $\text{Col}_{ob}$ , and (e) C16-tri-CTP at 80 °C in  $\text{Col}_{ob}$ .

### Electron density maps (EDMs)

Electron density maps (EDMs) can provide a visualized scenario of electron density distributions, thus corroborating the proposed structures or to some extent amending possible deviations of the structure assignments.<sup>58–61</sup> As shown in Fig. 5, EDMs were reconstructed from the measured SAXS intensities for complexes C10-tri-CTP, C14-tri-CTP and C16-tri-CTP in their columnar LC mesophases of  $\text{Col}_r$  or  $\text{Col}_{ob}$ . EDMs showed that the reddish orange oval regions with the highest electron density in both  $\text{Col}_r$  and  $\text{Col}_{ob}$  were concentrated in the center of the column, with the six violet areas of the lowest electron density discretely distributed around the periphery of the column. A comparison of EDMs for the ILC complexes also allowed us to locate molecular building blocks in the corresponding supramolecular columnar structure. As shown in Fig. 5b, the shorter axis length of the central high-density oval part was about 0.77 nm, which was in good agreement with the contour diameter of the TP unit of 0.74 nm as estimated from its conformation by Chem3D software. Meanwhile, the thickness of the medium density areas around the central ellipsoid was also in accordance with the size of crown ether, which further corroborated its columnar stacking structure. The longer axis of the central

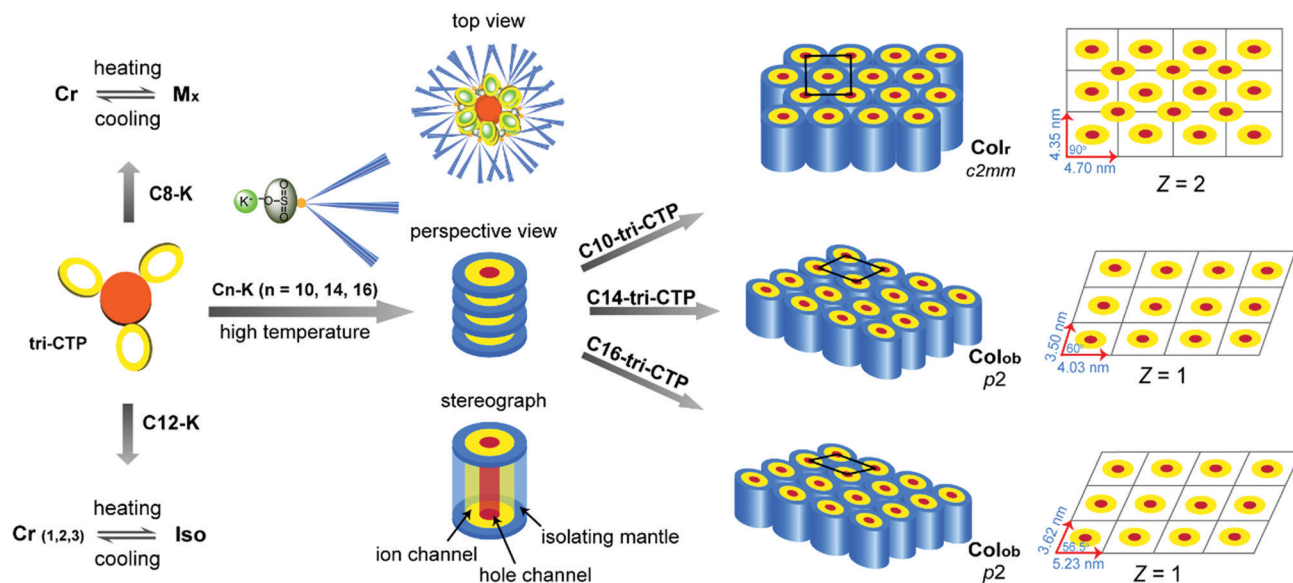


Fig. 4 Schematic illustration of the series of ionic LC complexes with proposed packing structures of 2D discotic columnar mesophases composed of molecule cables with a central TP-stacking electron/hole hopping conduction channel and a surrounding ion channel through a facile supramolecular approach of host-guest complexation.

ellipsoid in all three EDMs was different and increased slightly with the lengthening of the alkyl tails, which indicated that the stacking of tri-CTP cores within the column was not simply overlapped, but stacking with a certain degree of dislocation. Such a stacking character was consistent with the measured results that the ionic conductivity decreased with the increased alkyl tails of the ILC complexes. From the stacking structure as shown in Fig. 5b, it is clear that the mono- or di-alkyl substituted systems will lead to unfavorable space packing with overmuch vacancies, which helps us to understand the transition from the monotropic mesophases of mono- or di-alkyl based complexes<sup>56</sup> into the enantiotropic columnar LC phases of the tri-alkyl

substituted systems and the significant improvement of thermal stability. Moreover, the composition and proportion between the nonpolar flexible alkyl moiety and the polar core composed of rigid aromatic TP and host-guest  $K^+$ /crown ether directly affected the phase structure and its degree of order. Though at present we still cannot fully understand why an ordered polycrystalline phase was always formed for C12-tri-CTP in sharp contrast to the columnar LC mesophases for other analogous complexes with shorter or longer alkyl tails, it was presumably that the tri-dodecyloxy tails with flexibility and nonpolarity and the core moieties of rigid and polar nature might be exactly in an ideal balance for the complex of C12-tri-CTP, leading to formation of a highly ordered structure in polycrystalline solid state.

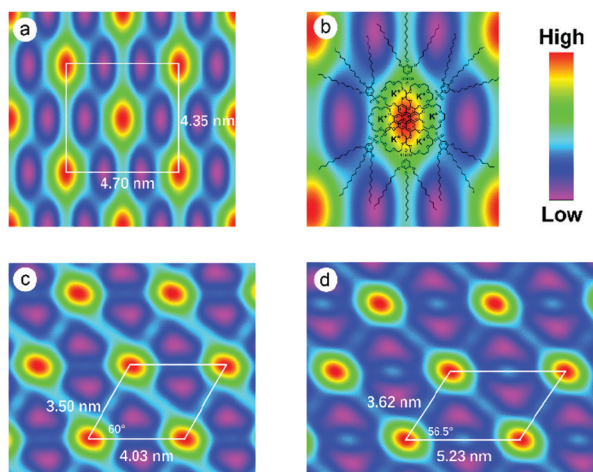
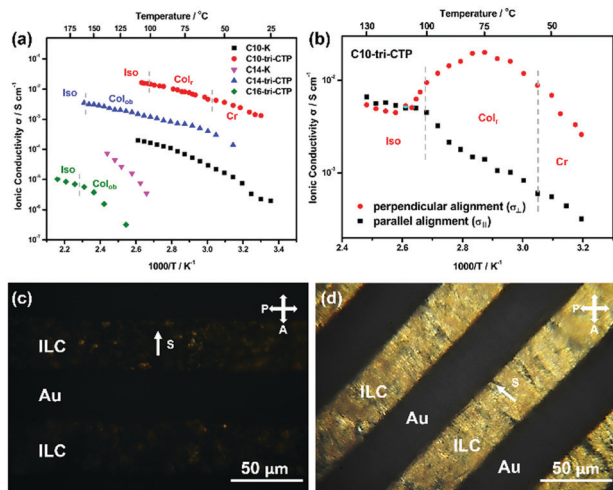


Fig. 5 The reconstructed electron density maps (EDMs) for the complexes of (a) C10-tri-CTP, Col<sub>r</sub>, 80 °C; (b) a single supramolecular column with the suggested molecular stacking mode for C10-tri-CTP; (c) C14-tri-CTP, Col<sub>ob</sub>, 80 °C; and (d) C16-tri-CTP, Col<sub>ob</sub>, 80 °C, with proposed lattice parameters based on SAXS/WAXS analyses.

### Anisotropic ionic conductivities

We explored and determined the ionic conductivities of the columnar ILC complexes with the alternating current impedance method adopting interdigital gold electrodes as reported by Kato and coworkers.<sup>8,36,58,62–64</sup> Fig. 6a shows the ionic conductivities of the unoriented polydomain thin films of C10-tri-CTP, C14-tri-CTP and C16-tri-CTP as a function of temperature. For comparison, the temperature-dependent ionic conductivities of the neat guest potassium trialkoxybenzenesulfonates of C10-K and C14-K were also measured (for representative electrochemical AC impedance curves see Fig. S20 (ESI<sup>†</sup>), with variable temperature ionic conductivities summarized in Table S4, ESI<sup>†</sup>). However, the effective ionic conductivities of C8-tri-CTP and C12-tri-CTP could not be detected as a result of C8-tri-CTP in a relatively ill-organized mesophase and C12-tri-CTP always in its polycrystalline state before melting into isotropic liquid, which implied either not forming or severely blocking effective channels for ion transport. Similarly, in the crystalline region of C14-tri-CTP and C16-tri-CTP at room temperature, the ionic conductivities were too low to be



**Fig. 6** (a) Ionic conductivities as a function of temperature of the series of ILC complexes of C10-tri-CTP, C14-tri-CTP, and C16-tri-CTP, in the unoriented polydomain thin films with a heating rate of  $5^{\circ}\text{C min}^{-1}$ , together with those of the guest compounds of C10-K and C14-K for comparison. (b) Ionic conductivities of C10-tri-CTP thin films in uniaxial orientation with the columns in the  $\text{Col}_{\text{r}}$  state aligned parallel ( $\sigma_{\parallel}$ ) or perpendicular ( $\sigma_{\perp}$ ) to the interdigital electrodes through shearing. POM images of the perpendicularly aligned ( $\sigma_{\perp}$ ) C10-tri-CTP thin film in the dark (c) or under brightness (d) under crossed polarizers periodically changed upon rotating every  $45^{\circ}$ , with the shearing direction (S), polarizer (P) and analyzer (A) indicated by single or two-way arrows.

observably detected. However, the ionic conductivity of C10-tri-CTP at room temperature can be well measured, reaching a value of  $1.32 \times 10^{-3} \text{ S cm}^{-1}$ . With an increase in temperature, the conductivities of the complexes increased gradually, when entering the temperature range of columnar LC mesophases, reaching a quite high level beyond  $10^{-2} \text{ S cm}^{-1}$  for the C10-tri-CTP complex. The temperature dependence and the increasing tendency of the ionic conductivities during the transition from the crystalline to LC mesophase state were in agreement with those disclosed by Kato *et al.* based on ILCs<sup>36,62–65</sup> and by Percec *et al.* from the supra-molecular cylindrical channel-like architectures based on complexation of the dendron-substituted crown ether and alkali metal salts.<sup>66</sup> As shown in Fig. 6a, the ionic conductivities of the neat guest C10-K were 2–3 orders of magnitude lower than those of the corresponding complex C10-tri-CTP at the same temperature. For the guest C14-K with longer alkyl tails, the ionic conductivities could not be measured at room temperature because of its excessive resistance. At higher temperatures, the ionic conductivities of C14-K were 1–2 orders of magnitude lower than those of the C14-tri-CTP complex. Therefore, the formation of columnar ion channels in the ILC complexes indeed played a decisive role in remarkably enhancing the ionic conductivities, which is more prominently judged from the anisotropic ionic conductivity test as presented below.

Furthermore, anisotropic ionic conductivities were measured for the macroscopically aligned thin films of C10-tri-CTP and C14-tri-CTP in their columnar mesophases (Table S5, ESI<sup>†</sup>). A uniaxial orientation was achieved in two directions, with the columnar mesophases aligned either parallel ( $\sigma_{\parallel}$ ) or perpendicular

( $\sigma_{\perp}$ ) to the interdigital electrodes by applying a shearing force in the oriented films as confirmed by the changed POM images rotating every  $45^{\circ}$  (Fig. 6c and d). It is worth mentioning that here the ion transport was in parallel to the columns in the perpendicularly aligned ( $\sigma_{\perp}$ ) thin films, and across the columns in the parallel aligned ( $\sigma_{\parallel}$ ) cases. For C10-tri-CTP, as shown in Fig. 6b, the perpendicularly aligned ( $\sigma_{\perp}$ ) conductivities were 10–15 times higher than those of the parallel aligned ( $\sigma_{\parallel}$ ). The conductivity gap between  $\sigma_{\perp}$  and  $\sigma_{\parallel}$  only slightly changed with the increase of temperature until over  $80^{\circ}\text{C}$ , and then decreased gradually until the gap disappeared showing almost the same conductivities for the  $\sigma_{\parallel}$  and  $\sigma_{\perp}$  aligned samples upon the increase in temperature up to  $107^{\circ}\text{C}$ , which was beyond the clearing point temperature and resulted in the breakup of the columnar ionic channels. The anisotropic behavior of complex C14-tri-CTP was similar to that of C10-tri-CTP, with the ionic conductivities in parallel to the columns ( $\sigma_{\perp}$ ) being about 2–6 times higher than those across the columns ( $\sigma_{\parallel}$ ) at temperatures below  $100^{\circ}\text{C}$ , and then the difference decreased upon heating, and finally merged at temperatures higher than  $150^{\circ}\text{C}$  with transition into the isotropic state (Fig. S21 and S22, ESI<sup>†</sup>). Similar anisotropic behaviors of ionic conductivity were impressively demonstrated by Kato and coworkers from various columnar ILC systems.<sup>8,36,58,62–64</sup>

From the ionic conductivity performance comparison of three columnar ILC complexes, it can be concluded that the ionic conductivities of C14-tri-CTP and C16-tri-CTP in oblique columnar mesophase  $\text{Col}_{\text{ob}}$  are markedly lower than that of C10-tri-CTP in  $\text{Col}_{\text{r}}$  of the center-faced rectangular columnar structure, which is mainly ascribed to the following two points: (1) the tri-CTP cores stacked with an increased degree of dislocation with the length increase of alkyl tails, which resulted in the correspondingly increased structural distortion of assembled ionic channels and thus the decrease of ionic conductivities, as similarly reported for various columnar mesophase transformations and difference in conductivities by Kato and coworkers.<sup>58,59,64</sup> (2) Since the ionic conductivities of organic ionic conductors increase with increased ionic content,<sup>36,62</sup> the decreasing tendency of the ionic conductivities of the ILC complexes of C10-tri-CTP, C14-tri-CTP and C16-tri-CTP is consistent with the increased proportions of the non-conductive alkyl moieties. These results further confirmed the efficiency of 1D ion transport channels in various self-organized columnar mesophases of  $\text{Col}_{\text{r}}$  and  $\text{Col}_{\text{ob}}$ , with the orientation direction being regulated simply through a directed shearing.

It is worth pointing out that the adoption of sulfonic counterions here is also an important factor that cannot be ignored, because our preliminary comparative study with the sulfonic replaced by carboxylic counterions only showed that the conductivities of the complexes from tri-CTP and potassium trialkoxy gallate with various alkyl tails were remarkably reduced as low as almost impossible to be detected even at elevated temperatures, which was mainly attributed to the formation of much closer ion pairs between potassium and carboxyl counterions, thus seriously hindering the ion transport. It is very encouraging to notice that the measured ionic

conductivities of  $1.32 \times 10^{-3} \text{ S cm}^{-1}$  at room temperature and  $1.48 \times 10^{-2} \text{ S cm}^{-1}$  at  $100^\circ\text{C}$  for the trialkoxybenzenesulfonate based complex of C10-tri-CTP in the unoriented polydomain thin films even reached  $1.99 \times 10^{-2} \text{ S cm}^{-1}$  at  $75^\circ\text{C}$  in uniaxial orientation with the columns in the  $\text{Col}_r$  state aligned perpendicular ( $\sigma_{\perp}$ ) to the interdigital electrodes (Fig. 6, and Tables S4 and S5, ESI†), which has met the requirements for solid state electrolytes competent for applications in commercial batteries ( $10^{-3}$ – $10^{-2} \text{ S cm}^{-1}$ ).<sup>67</sup> Recently, as a new generation of alkali metal batteries, potassium ion batteries (PIBs) have attracted much attention due to their more abundant reserve and economic advantage of the element potassium as compared to lithium.<sup>68,69</sup> However, the study of solid electrolytes for PIBs is still in its infancy as compared to  $\text{Li}^+$  or  $\text{Na}^+$  ionic batteries,<sup>68–70</sup> because the ionic conductivity of common solid electrolytes for  $\text{K}^+$  is relatively low for the much larger size of  $\text{K}^+$  as compared to  $\text{Li}^+$ , which is one of the main factors restricting the development of PIBs. Here the supramolecular discotic ILCs, showing very high ionic conductivities thanks to the potassium ion channels based on columnar mesophases, are expected to be applied as solid-state electrolytes in PIBs, and further work related to this is underway.

### Electrochemical properties and charge carrier mobilities

The C10-tri-CTP, C14-tri-CTP and C16-tri-CTP complexes and the host compound tri-CTP were first investigated with cyclic voltammetry (CV) to determine the approximate energy values of their HOMO frontier orbitals with ferrocene as the reference (Fig. S23, ESI†). Optical HOMO–LUMO gap energies ( $E_g$ ) were determined by UV-Vis spectroscopy both in solution and in film (Fig. S23, ESI†), as presented in Table 2, together with the values obtained by CV, while the LUMO levels of all investigated samples were calculated from HOMO energy and  $E_g$  values measured in solution, referring to the literature method.<sup>71,72</sup> All compounds showed quasi-reversible oxidation peaks but no reduction peaks in the observed electrochemical window (–2 to 2 V). The obtained HOMO, LUMO and  $E_g$  values of tri-CTP and complexes C10-tri-CTP, C14-tri-CTP and C16-tri-CTP were in good agreement with those reported values for triphenylene-ether derivatives,<sup>71,72</sup> while  $E_g$  values of the complex series in the film reduced below 3 eV mainly due to

**Table 2** Oxidation potentials determined by CV and optical HOMO–LUMO gaps of the  $C_n$ -tri-CTP complexes ( $n = 10, 14, 16$ ) and the host compound tri-CTP

Compound	1st Ox $E_{\text{onset}}^a/\text{V}$	HOMO <sup>b</sup> / eV	LUMO <sup>c</sup> / eV	$E_g^d$ (in solution)/ eV	$E_g^d$ (in film)/ eV
C10-tri-CTP	0.84	–5.29	–1.58	3.71	2.36
C14-tri-CTP	0.82	–5.27	–1.57	3.70	2.86
C16-tri-CTP	0.90	–5.35	–1.63	3.72	2.94
Tri-CTP	0.98	–5.43	–1.70	3.73	—

<sup>a</sup>  $E_{\text{Ox-onset}}$  in V vs. Ag/AgCl with a glassy carbon working electrode in DCM. <sup>b</sup>  $E_{\text{HOMO}}$  in eV =  $-e[E_{\text{Ox-onset}} - 0.35 \text{ V}] - 4.8 \text{ eV}$  (0.35 V is the  $E_{\text{Ox-onset}}$  of ferrocene/ferrocenium (Fc/Fc<sup>+</sup>) versus Ag/AgCl). <sup>c</sup> Calculated from HOMO energy and optical gap in DCM solution. <sup>d</sup> Optical energy gap ( $E_g$ ) in DCM solution and film.

$\pi$ - $\pi$  interactions between conjugated aromatic cores in the solid state and slightly increased with the lengthening of alkyl tails, which implied a correlation with their charge carrier mobility performance.

To further verify the optoelectronic properties of ILC complexes, their charge carrier mobilities were evaluated by time-of-flight (TOF) measurements. The TOF technique possesses some advantages such as simplicity of preparation and intuitive data analysis reflecting the long-range carrier mobility, which is much closer to the real environment for applications. Therefore, the TOF test results are more meaningful and widely used for optoelectronic performance evaluation.<sup>15,19,20,73–83</sup> The adopted laser pulse of wavelength 337 nm is near the absorption shoulder peak of the UV-vis spectra for the  $C_n$ -tri-CTP ( $n = 10, 14, 16$ ) complexes in thin films (Fig. S24, ESI†). The electron mobility of the TP-based ILC complexes was too low to be detected by the TOF equipment used. With an applied reverse bias voltage of 20 V, the representative photocurrent curves and temperature dependence of the hole mobilities for the ILC complexes measured by TOF are shown in Fig. 7 and in the ESI† (Tables S6–S8). The hole mobilities of C10-tri-CTP, C14-tri-CTP and C16-tri-CTP at room temperature in their crystalline state were measured to be in the range from  $10^{-3}$  to  $10^{-2} \text{ cm}^2 \text{ V}^{-1} \text{ s}^{-1}$ . With the increase of temperature, the ILC complexes transformed into ordered 2D columnar structures, resulting in the better establishment of transport channels, and thus the hole mobilities increased significantly, reaching  $10^{-2}$  to  $10^{-1} \text{ cm}^2 \text{ V}^{-1} \text{ s}^{-1}$  for the annealed samples in their homeotropically aligned columnar mesophases. The temperature dependence of hole mobilities as

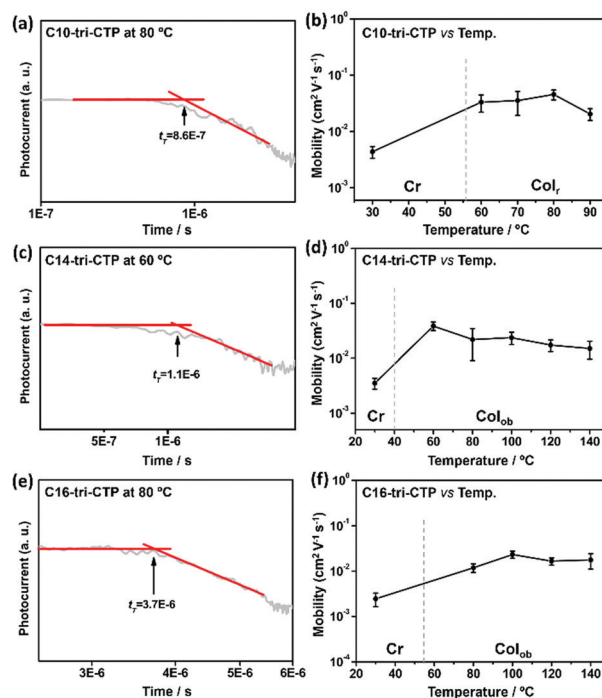


**Fig. 7** The representative photocurrent curves with a laser pulse at 337 nm (indicated with the test temperature) and temperature dependence of TOF measured hole mobilities for the ILC complexes of (a and b) C10-tri-CTP, (c and d) C14-tri-CTP, and (e and f) C16-tri-CTP.

measured by the TOF technique of the ILC complex series was largely consistent with their thermal behaviors and phase transition trends, thus precluding the possible interference or artificial signals from ion migration the carrier mobility of which increased monotonously with temperature, conforming to the general characteristics of hole transport.<sup>84–86</sup> It should be noted that in sharp contrast to the inspiring performance of annealed samples, those upon cooling rapidly into the LC temperature region from the isotropic melts failed to be detected due to the lack of sufficient non-discrete photocurrent signals. Therefore, adequate annealing to realize the desired homeotropic alignment and establish suitable conduction pathways is an indispensable key procedure for such columnar ILC complexes to achieve high hole transport performance.

Molecular packing is believed to be another key point for determining and regulating the performance of organic and polymeric optoelectronic materials.<sup>87</sup> Here, the improved hole mobilities of  $10^{-2}$  to  $10^{-1}$   $\text{cm}^2 \text{V}^{-1} \text{s}^{-1}$  achieved by the discotic ILC complexes with tri-CTP cores in columnar mesophases are comparable to those reported for the corresponding modified alkoxy TP discotic monomers or dimers,<sup>19,20,77–79</sup> indicating more efficient packing of the aromatic TP moieties in virtue of the host–guest interactions between the attached crown ether and potassium cations.<sup>40,41,44,45,57,88,89</sup> Such readily prepared ILC complexes with good thermal stability in their properly aligned ordered columnar structures exhibit fantastic dual-channel transport properties both for ions and holes, which are very attractive and hopeful to be developed as promising organic electronic materials satisfying some specific requirements, such as acting as versatile solid-state electrolytes in PIBs or in dye sensitized solar cells (DSSCs).<sup>90,91</sup>

## Conclusions

In conclusion, a series of supramolecular discotic ILCs of *C<sub>n</sub>*-tri-CTP have been produced through host–guest interactions together with  $\pi$ – $\pi$  stacking and electrostatic interactions between the readily prepared electrically neutral tri-CTP and the facily available potassium trialkoxybenzenesulfonates with different length alkyl tails of carbon number  $n = 8, 10, 12, 14, 16$ . The thus obtained ILC complexes exhibited enantiotropic ordered columnar mesophases with broad LC temperature ranges and excellent thermal stability as characterized by TGA, DSC, POM and SAXS/WAXS. Such as for C10-tri-CTP at 80 °C in the LC state, a center-faced rectangular columnar LC mesophase ( $\text{Col}_r$ ,  $C2mm$ ) was constructed, and for the complexes with longer alkyl tails of C14-tri-CTP and C16-tri-CTP at 80 °C, oblique columnar mesophases ( $\text{Col}_{ob}$ ,  $P2$ ) were generated with some different lattice parameters.

Ionic conductivities of some selected columnar ILC complexes have been measured *via* the alternating current impedance method to show impressive high values of several orders higher than those of the corresponding neat guest potassium trialkoxybenzenesulfonates, and increased with elevated temperature to enter the columnar LC mesophases. High anisotropic ionic conductivities were achieved for the macroscopically aligned ILC complex thin films of C10-tri-CTP and C14-tri-CTP in their

columnar mesophases simply by directed shearing, with the conductivities aligned perpendicularly to the electrode ( $\sigma_{\perp}$ ) being many times higher than those of the parallel aligned ( $\sigma_{\parallel}$ ). Moreover, the hole mobilities of the ILC complexes C10-tri-CTP, C14-tri-CTP and C16-tri-CTP in the homeotropically aligned columnar mesophases after annealing as evaluated with the TOF technique reached rather high levels in the order of  $10^{-2}$  to  $10^{-1}$   $\text{cm}^2 \text{V}^{-1} \text{s}^{-1}$ . Therefore, the supramolecular discotic ILC complexes in ordered columnar structures after proper alignment exhibited simultaneously rather high ionic conductivities and hole mobilities, such fantastic dual-channel transporting characteristics of both ions and holes should be very hopeful for their development as versatile organic electronic materials for many promising unique applications.

## Experimental section

### Instrumentation

<sup>1</sup>H NMR and <sup>13</sup>C NMR spectra in solution were obtained using 400 MHz (Bruker DRX400) instruments. Electrospray ionization mass spectra (ESI-MS) were obtained on a LCMS-2020 single quadrupole mass spectrometer (Shimadzu). Differential scanning calorimetry (DSC) thermograms were recorded on a Mettler-Toledo DSC I calorimeter equipped with a cooling accessory and under a N<sub>2</sub> atmosphere. Typically, about 8 mg of the solid sample was encapsulated in a sealed aluminum pan with an identical empty pan as the reference. Indium was used as a calibration standard. The polarized optical microscope equipped with a Leitz-350 heating stage and a Nikon (D3100) digital camera was used to characterize thermal transitions, and observe and photograph various LC or crystalline textures. The samples were prepared by melt-pressing and sandwiched between two glass plates. X-ray scattering experiments were performed with a high-flux small-angle X-ray scattering instrument (SAXSess mc<sup>2</sup>, Anton Paar) equipped with a Kratky block-collimation system and temperature control units (Anton Paar TCS 120 and TCS 300). Both small angle X-ray scattering (SAXS) and wide angle X-ray scattering (WAXS) were simultaneously performed on an imaging-plate (IP) which extended to the high-angle range (the  $q$  range covered by the IP was from 0.06 to 29  $\text{nm}^{-1}$ ,  $q = 4\pi \sin \theta / \lambda$ , where wavelength  $\lambda$  is 0.1542 nm for Cu-K $\alpha$  radiation and  $2\theta$  is the scattering angle) at 40 kV and 50 mA. The powder samples were encapsulated with aluminum foil for the measurement and the obtained X-ray analysis data were processed with the associated SAXSquant software 3.80. UV-vis spectra of thin film samples were recorded using a Shimadzu UV3600 UV-vis spectrophotometer. The thin films for UV-vis tests were typically prepared by spin-coating the sample chloroform solution (100 mg solid in 2 mL CHCl<sub>3</sub>) on quartz substrates (2.0 cm  $\times$  2.0 cm) at 800 rpm, and then the prepared thin films were annealing at 60 °C for 6 h before UV-vis tests.

### Reconstruction of electron density maps (EDMs)

Two-dimensional electron density maps<sup>58–61</sup> were reconstructed on the basis of the general formula:

$$\rho(x,y) = \sum F(hk) \exp[i2\pi(hx + ky)]$$

Here  $F(hk)$  is the structure factor of a diffraction peak with index  $(hk)$ . The experimentally observed diffraction intensity is given by:

$$I(hk) = K \cdot F(hk) \cdot F^*(hk) = K \cdot |F(hk)|^2$$

where  $K$  is a constant related to the sample volume, incident beam intensity *etc.* In this work only the relative electron densities are concerned, hence this constant is simply set to 1. Thus the electron density is calculated according to the equation:

$$\rho(xy) = \sum \text{sqrt}[I(hk)] \exp[i2\pi(hx + ky) + \phi_{hk}]$$

where  $\phi_{hk}$  is the phase angle of the  $hk$  Bragg reflection. As the observed diffraction intensity  $I(hk)$  is only related to the amplitude of the structure factor  $|F(hk)|$ , the information about the phase of  $F(hk)$ ,  $\phi_{hk}$ , cannot be determined directly from the experimental results. However, the problem is significantly simplified with most space group symmetries, where the phase angle  $\phi_{hk}$  of the given  $(hk)$  reflection is limited to 0 or  $\pi$ .

### Dynamic ionic conductivity (DIC) measurements

The ionic conductivity was measured using a VersaSTAT 3F (aka, V3F) Princeton Electrochemical Workstation equipped with a Leitz-350 hot stage and VersaStudio software, with parameters of an amplitude of 0.3 V, the frequency range of 100 Hz–1 MHz and a heating rate of 5 °C min<sup>-1</sup>. In order to ensure the reliability of the electrodes, temperatures involved in our experiments were all below 200 °C. The surface of the interdigital electrodes was cleaned with ethanol before use. Then the resistance of the interdigital electrodes was monitored with a multimeter to guarantee the insulating characteristic. The samples were evenly applied on the surface of the interdigital electrodes and then heated slowly to the clearing point at a rate of 10 °C min<sup>-1</sup>. Then the composite was covered with a glass slide and slightly pressed to form a homogeneous film on the surface of the electrode without any crack or air bubbles, followed by cooling to room temperature at a rate of 20 °C min<sup>-1</sup>. The working electrode of the electrochemical workstation was connected to one of the interdigital electrodes, and the reference electrode was connected to the other one. The open circuit voltage in the preparation was measured to be 0.3 V. Subsequently, the impedance was measured using the AC impedance test mode with parameters of an amplitude of 0.3 V, an initial frequency of 100 Hz and a terminal frequency of 1 MHz. With the whole test device placed on the hot stage, the impedance values were measured every 5–10 °C. The testing process and adopted method for the conductivity calculation were similar to that reported by Kato and coworkers.<sup>62–64</sup>

### Electrochemical measurements

All cyclic voltammetry (CV) measurements were recorded with a CHI-760e electrochemical workstation (CH Instruments Ins., Shang Hai, China). The current–voltage ( $I$ – $V$ ) curves were recorded by sweeping the voltage with a scan rate of 100 mV s<sup>-1</sup> and a sampling frequency of 60 kHz. A glassy carbon electrode as a working electrode; Ag/AgCl as a reference electrode; and the

platinum wire as a counter electrode were used. Typically, 20 mg of complex  $C_n$ -tri-CTP ( $n = 10, 14, 16$ ) was added into 10 mL CH<sub>2</sub>Cl<sub>2</sub> with 0.1 M tetrabutylammonium hexafluorophosphate. The  $E_g$  values were determined from UV-vis spectra through extrapolating the linear region to zero absorption.<sup>71</sup>

### Charge transport measured by time of flight (TOF)

The hole mobilities  $\mu$  of the complexes were measured using a TOF-401 device. LC cells (E.H.C. Company, Japan) with semi-transparent indium tin oxide (ITO) electrodes were loaded with the samples *via* the capillary effect in their isotropic melts and then cooled very slowly or annealed in the selected temperature to obtain highly ordered LC films. The thus-prepared cells were then illuminated with light pulses from a N<sub>2</sub> laser (USHO KEC 160, wavelength = 337 nm, pulse width = 1000 ps). Simultaneously, the transient photocurrent across the cell at an external bias voltage supplied with a power unit (Kikusui PAN110-3A) was amplified using a NF low-digital phosphor oscilloscope (Tektronix TDS 3032C). The transit time  $t_T$  of the photo-generated charge carriers travelling on the LC layer was determined from the inflection point of a double-logarithmic plot of transient photocurrent as a function of time. Then the mobility was calculated according to:

$$\mu = d^2/Vt_T = d/Et_T$$

where  $d$  is the thickness of the charge-transport layer (*ca.* 9  $\mu\text{m}$ ),  $V$  is the applied bias voltage, and  $E$  is the electric field strength.

### Conflicts of interest

There are no conflicts to declare.

### Acknowledgements

This work was supported by the National Natural Science Foundation of China (Grants No. 21875098 and 21574062) and also partially by the Program for Changjiang Scholars and Innovative Research Team in University (IRT\_16R38), and the Fundamental Research Funds for the Central Universities and the Scientific Research Foundation of Graduate School of Nanjing University (Grant 2017ZDL06). We express our sincere gratitude to Prof. Chunxiu Zhang at the Beijing Institute of Graphic Communication for her kind help in the TOF measurements and to Dr Huanjun Lu at Soochow University for her generous assistance in the reconstruction of EDMs.

### Notes and references

- 1 K. Binnemans, *Chem. Rev.*, 2005, **105**, 4148–4204.
- 2 K. Goossens, K. Lava, C. W. Bielawski and K. Binnemans, *Chem. Rev.*, 2016, **116**, 4643–4807.
- 3 C. F. J. Faul, *Acc. Chem. Res.*, 2014, **47**, 3428–3438.
- 4 Y. Haketa and H. Maeda, *Chem. Commun.*, 2017, **53**, 2894–2909.
- 5 S. Chen and S. H. Eichhorn, *Isr. J. Chem.*, 2012, **52**, 830–843.

- 6 K. V. Axenov and S. Laschat, *Materials*, 2011, **4**, 206–259.
- 7 S. K. Pal and S. Kumar, *Ionic Discotic Liquid Crystals: Recent Advances and Applications*, John Wiley & Sons, Inc., 2014.
- 8 T. Kato, M. Yoshio, T. Ichikawa, B. Soberats, H. Ohno and M. Funahashi, *Nat. Rev. Mater.*, 2017, **2**, 17001.
- 9 T. Wöhrle, I. Wurzbach, J. Kirres, A. Kostidou, N. Kapernaum, J. Litterscheidt, J. C. Haenle, P. Staffeld, A. Baro, F. Giesselmann and S. Laschat, *Chem. Rev.*, 2016, **116**, 1139–1241.
- 10 S. Sergeev, W. Pisula and Y. H. Geerts, *Chem. Soc. Rev.*, 2007, **36**, 1902–1929.
- 11 J. Wu, W. Pisula and K. Müllen, *Chem. Rev.*, 2007, **107**, 718–747.
- 12 S. Kumar, *Chemistry of Discotic Liquid Crystals: From Monomers to Polymers*, CRC Press, 2010.
- 13 S. Laschat, A. Baro, N. Steinke, F. Giesselmann, C. Hagele, G. Scalia, R. Judele, E. Kapatsina, S. Sauer, A. Schreivogel and M. Tosoni, *Angew. Chem., Int. Ed.*, 2007, **46**, 4832–4887.
- 14 S. K. Pal, S. Setia, B. S. Avinash and S. Kmar, *Liq. Cryst.*, 2013, **40**, 1769–1816.
- 15 B. Mu, X. Hao, J. Chen, Q. Li, C. Zhang and D. Chen, *Polym. Chem.*, 2017, **8**, 3286–3293.
- 16 E. M. García-Frutos, U. K. Pandey, R. Termine, A. Omenat, J. Barberá, J. L. Serrano, A. Golemme and B. Gómez-Lor, *Angew. Chem., Int. Ed.*, 2011, **50**, 7399–7402.
- 17 R. Chico, E. Domingo, C. Domínguez, B. Donnio, B. Heinrich, R. Termine, A. Golemme, S. Coco and P. Espinet, *Chem. Mater.*, 2017, **29**, 7587–7595.
- 18 J. De, I. Bala, S. P. Gupta, U. K. Pandey and S. K. Pal, *J. Am. Chem. Soc.*, 2019, **141**, 18799–18805.
- 19 J. Bi, H. Wu, Z. Zhang, A. Zhang, H. Yang, Y. Feng, Y. Fang, L. Zhang, Z. Wang, W. Qu, F. Liu and C. Zhang, *J. Mater. Chem. C*, 2019, **7**, 12463–12469.
- 20 K. C. Zhao, J. Q. Du, H. F. Wang, K. Q. Zhao, P. Hu, B. Q. Wang, H. Monobe, B. Heinrich and B. Donnio, *Chem. – Asian J.*, 2019, **14**, 462–470.
- 21 I. Bala, J. De, S. P. Gupta, H. Singh, U. K. Pandey and S. K. Pal, *Chem. Commun.*, 2020, **56**, 5629–5632.
- 22 E. Domingo, C. L. Folcia, J. Ortega, J. Etxebarria, R. Termine, A. Golemme, S. Coco and P. Espinet, *Inorg. Chem.*, 2020, **59**, 10482–10491.
- 23 S. Jhulki, J. Kim, I. C. Hwang, G. Haider, J. Park, J. Y. Park, Y. Lee, W. Hwang, A. A. Dar, B. Dhara, S. H. Lee, J. Kim, J. Y. Koo, M. H. Jo, C. C. Hwang, Y. H. Jung, Y. Park, M. Kataria, Y. F. Chen, S. H. Jhi, M. H. Baik, K. Baek and K. Kim, *Chem*, 2020, **6**, 1–11.
- 24 M. A. Alam, J. Motoyanagi, Y. Yamamoto, T. Fukushima, J. Kim, K. Kato, M. Takata, A. Saeki, S. Seki, S. Tagawa and T. Aida, *J. Am. Chem. Soc.*, 2009, **131**, 17722–17723.
- 25 J. J. Lee, A. Yamaguchi, M. A. Alam, Y. Yamamoto, T. Fukushima, K. Kato, M. Takata, N. Fujita and T. Aida, *Angew. Chem., Int. Ed.*, 2012, **51**, 8490–8494.
- 26 H. Maeda, K. Naritani, Y. Honsho and S. Seki, *J. Am. Chem. Soc.*, 2011, **133**, 8896–8899.
- 27 B. Dong, T. Sakurai, Y. Honsho, S. Seki and H. Maeda, *J. Am. Chem. Soc.*, 2013, **135**, 1284–1287.
- 28 Y. Zakrevskyy, C. F. J. Faul, Y. Guan and J. Stumpe, *Adv. Funct. Mater.*, 2004, **14**, 835–841.
- 29 D. Wu, W. Pisula, V. Enkelmann, X. Feng and K. Müllen, *J. Am. Chem. Soc.*, 2009, **131**, 9620–9621.
- 30 J. Kadam, C. F. J. Faul and U. Scherf, *Chem. Mater.*, 2004, **16**, 3867–3871.
- 31 F. Camerel, G. Ulrich, J. Barberá and R. Ziessel, *Chem. – Eur. J.*, 2007, **13**, 2189–2200.
- 32 D. Wu, L. Zhi, G. J. Bodwell, G. Cui, N. Tsao and K. Müllen, *Angew. Chem., Int. Ed.*, 2007, **46**, 5417–5420.
- 33 Y. Luo, N. Marets and T. Kato, *Chem. Sci.*, 2018, **9**, 608–616.
- 34 T. Kato, J. Uchida, T. Ichikawa and T. Sakamoto, *Angew. Chem., Int. Ed.*, 2018, **57**, 4355–4371.
- 35 L. Yang, X. Tan, Z. Wang and X. Zhang, *Chem. Rev.*, 2015, **115**, 7196–7239.
- 36 H. Shimura, M. Yoshio, K. Hoshino, T. Mukai, H. Ohno and T. Kato, *J. Am. Chem. Soc.*, 2008, **130**, 1759–1765.
- 37 P. Wei, X. Yan and F. Huang, *Chem. Soc. Rev.*, 2015, **44**, 815–832.
- 38 J. Li, D. Yim, W. D. Jang and J. Yoon, *Chem. Soc. Rev.*, 2017, **46**, 2437–2458.
- 39 J. J. Zhang, H. Y. Qiu, T. He, Y. Li and S. C. Yin, *Front. Chem.*, 2020, **8**, 560.
- 40 H. Engelkamp, S. Middelbeek and R. J. M. Nolte, *Science*, 1999, **284**, 785–788.
- 41 C. F. van Nostrum, S. J. Picken, A. J. Schouten and R. J. M. Nolte, *J. Am. Chem. Soc.*, 1995, **117**, 9957–9965.
- 42 Y. Ma, T. Marszalek, Z. Yuan, R. Stangenberg, W. Pisula, L. Chen and K. Müllen, *Chem. – Asian J.*, 2015, **10**, 139–143.
- 43 A. Schultz, S. Laschat, A. Saipa, F. Gießelmann, M. Nimtz, J. L. Schulte, A. Baro and B. Miehlich, *Adv. Funct. Mater.*, 2004, **14**, 163–168.
- 44 M. Kaller, C. Deck, A. Meister, G. Hause, A. Baro and S. Laschat, *Chem. – Eur. J.*, 2010, **16**, 6326–6337.
- 45 M. Kaller, S. Tussetschläger, P. Fischer, C. Deck, A. Baro, F. Gießelmann and S. Laschat, *Chem. – Eur. J.*, 2009, **15**, 9530–9542.
- 46 S. Laschat, A. Baro, T. Wöhrle and J. Kirres, *Liq. Cryst. Today*, 2016, **25**, 48–60.
- 47 K. Bader, M. M. Neidhardt, T. Wöhrle, R. Forschner, A. Baro, F. Gießelmann and S. Laschat, *Soft Matter*, 2017, **13**, 8379–8391.
- 48 M. Kaller and S. Laschat, *Top. Curr. Chem.*, 2012, **318**, 109–192.
- 49 G. Ungar, S. V. Batty, V. Percec, J. Heck and G. Johansson, *Adv. Mater. Opt. Electron.*, 1994, **4**, 303–313.
- 50 P. Staffeld, M. Kaller, P. Ehni, M. Ebert, S. Laschat and F. Giesselmann, *Crystals*, 2019, **9**, 74.
- 51 M. A. Shcherbina, A. V. Bakirov, U. Beginn, L. Yan, X. Zhu, M. Möller and S. N. Chvalun, *Chem. Commun.*, 2017, **53**, 10070–10073.
- 52 M. A. Shcherbina, A. V. Bakirov, L. Yan, U. Beginn, X. Zhu, M. Möller and S. N. Chvalun, *Mendeleev Commun.*, 2015, **25**, 142–144.

- 53 M. A. Shcherbina, A. V. Bakirov, A. N. Yakunin, U. Beginn, L. Yan, M. Möller and S. N. Chvalun, *Soft Matter*, 2014, **10**, 1746–1757.
- 54 S. Asaftei, M. Ciobanu, A. M. Lepadatu, E. Song and U. Beginn, *J. Mater. Chem.*, 2012, **22**, 14426–14437.
- 55 U. Beginn, L. Yan, S. N. Chvalun, M. A. Shcherbina, A. Bakirov and M. Möller, *Liq. Cryst.*, 2008, **35**, 1073–1093.
- 56 B. Mu, K. Chen, J. Chen, J. Fang and D. Chen, *Liq. Cryst.*, 2018, **45**, 1287–1293.
- 57 V. Percec, G. Johansson, G. Ungar and J. Zhou, *J. Am. Chem. Soc.*, 1996, **118**, 9855–9866.
- 58 B. Soberats, M. Yoshio, T. Ichikawa, X. Zeng, H. Ohno, G. Ungar and T. Kato, *J. Am. Chem. Soc.*, 2015, **137**, 13212–13215.
- 59 T. Ichikawa, M. Yoshio, A. Hamasaki, S. Taguchi, F. Liu, X. B. Zeng, G. Ungar, H. Ohno and T. Kato, *J. Am. Chem. Soc.*, 2012, **134**, 2634–2643.
- 60 F. Liu, B. Chen, U. Baumeister, X. Zeng, G. Ungar and C. Tschierske, *J. Am. Chem. Soc.*, 2007, **129**, 9578–9579.
- 61 X. Q. Liu, J. Wang, S. Yang and E. Q. Chen, *ACS Macro Lett.*, 2014, **3**, 834–838.
- 62 M. Yoshio, T. Mukai, H. Ohno and T. Kato, *J. Am. Chem. Soc.*, 2004, **126**, 994–995.
- 63 M. Yoshio, T. Kagata, K. Hoshino, T. Mukai, H. Ohno and T. Kato, *J. Am. Chem. Soc.*, 2006, **128**, 5570–5577.
- 64 S. Yazaki, Y. Kamikawa, M. Yoshio, A. Hamasaki, T. Mukai, H. Ohno and T. Kato, *Chem. Lett.*, 2008, **37**, 538–539.
- 65 T. Onuma, E. Hosono, M. Takenouchi, J. Sakuda, S. Kajiyama, M. Yoshio and T. Kato, *ACS Omega*, 2018, **3**, 159–166.
- 66 V. Percec, G. Johansson, J. Heck, G. Ungar and S. V. Battyb, *J. Chem. Soc., Perkin Trans. 1*, 1993, 1411–1420.
- 67 K. Murata, S. Izuchi and Y. Yoshihisa, *Electrochim. Acta*, 2000, **45**, 1501–1508.
- 68 X. Wu, D. P. Leonard and X. Ji, *Chem. Mater.*, 2017, **29**, 5031–5042.
- 69 H. Gao, L. Xue, S. Xin and J. B. Goodenough, *Angew. Chem., Int. Ed.*, 2018, **57**, 5449–5453.
- 70 Q. Yang, Z. Zhang, X. G. Sun, Y. S. Hu, H. Xing and S. Dai, *Chem. Soc. Rev.*, 2018, **47**, 2020–2064.
- 71 I. Seguy, P. Jolinat, P. Destruel, J. Farenc, R. Mamy, H. Bock, J. Ip and T. P. Nguyen, *J. Appl. Phys.*, 2001, **89**, 5442–5448.
- 72 S. J. Mahoney, M. M. Ahmida, H. Kayal, N. Fox, Y. Shimizuc and S. H. Eichhorn, *J. Mater. Chem.*, 2009, **19**, 9221–9232.
- 73 Q. Li, *Self-Organized Organic Semiconductors: From Materials to Device Applications*, John Wiley & Sons, 2011.
- 74 R. J. Bushby, S. M. Kelly and M. O'Neill, *Liquid Crystalline Semiconductors: Materials, Properties and Applications*, Springer, 2013.
- 75 D. Adam, P. Schuhmacher, J. Simmerer, L. Häussling, K. Siemensmeyer, K. H. Eitzbachi, H. Ringsdorf and D. Haarer, *Nature*, 1994, **371**, 141–143.
- 76 Y. Hirai, H. Monobe, N. Mizoshita, M. Moriyama, K. Hanabusa, Y. Shimizu and T. Kato, *Adv. Funct. Mater.*, 2008, **18**, 1668–1675.
- 77 Y. F. Wang, C. X. Zhang, H. Wu and J. L. Pu, *J. Mater. Chem. C*, 2014, **2**, 1667–1674.
- 78 X. Feng, L. Sosa-Vargas, S. Umadevi, T. Mori, Y. Shimizu and T. Hegmann, *Adv. Funct. Mater.*, 2015, **25**, 1180–1192.
- 79 Y. F. Wang, C. X. Zhang, H. Wu, A. Zhang, J. C. Wang, S. F. Zhang and J. L. Pu, *Soft Matter*, 2015, **11**, 712–718.
- 80 Y. Zeng, L. Lu, T. Gao, Y. Feng, J. F. Zheng, E. Q. Chen and X. K. Ren, *Dyes Pigm.*, 2018, **152**, 139–145.
- 81 X. Guo, Q. Gong, J. Borowiec, S. Zhang, S. Han, M. Zhang, M. Willis, T. Kreouzis and K. Yu, *ACS Appl. Mater. Interfaces*, 2019, **11**, 37184–37192.
- 82 A. Musiienko, P. Moravec, R. Grill, P. Praus, I. Vasylenko, J. Pekarek, J. Tisdale, K. Ridzonova, E. Belas, L. Landová, B. Hu, E. Lukosi and M. Ahmadi, *Energy Environ. Sci.*, 2019, **12**, 1413–1425.
- 83 A. Shah, B. Duponchel, A. Gowda, S. Kumar, M. Becuwe, C. Davoisne, C. Legrand, R. Doualia and D. P. Singh, *New J. Chem.*, 2020, **44**, 14872–14878.
- 84 T. Kreouzis, D. Poplavskyy, S. M. Tuladhar, M. Campoy-Quiles, J. Nelson, A. J. Campbell and D. D. C. Bradley, *Phys. Rev. B*, 2006, **73**, 1–15.
- 85 N. Yoshimoto and J. Hanna, *Adv. Mater.*, 2002, **14**, 988–991.
- 86 M. Funahashi and J. I. Hanna, *Phys. Rev. Lett.*, 1997, **78**, 2184–2187.
- 87 Q. Q. Li and Z. Li, *Acc. Chem. Res.*, 2020, **53**, 962–973.
- 88 M. Kaller, P. Staffeld, R. Haug, W. Frey, F. Giesselmann and S. Laschat, *Liq. Cryst.*, 2011, **38**, 531–553.
- 89 N. Steinke, M. Kaller, M. Nimtz, A. Baro and S. Laschat, *Liq. Cryst.*, 2010, **37**, 1139–1149.
- 90 A. Midya, Z. Xie, J. X. Yang, Z. K. Chen, D. J. Blackwood, J. Wang, S. Adams and K. P. Loh, *Chem. Commun.*, 2010, **46**, 2091–2093.
- 91 D. Högberg, B. Soberats, S. Uchida, M. Yoshio, L. Kloo, H. Segawa and T. Kato, *Chem. Mater.*, 2014, **26**, 6496–6502.